

# Multi-Channel Deep Networks for Block-Based Image Compressive Sensing

Siwang Zhou, *Member, IEEE*, Yan He, Yonghe Liu, and Chengqing Li, *Senior Member, IEEE*,

**Abstract**—Incorporating deep neural networks in image compressive sensing (CS) receives intensive attentions recently. As deep network approaches learn the inverse mapping directly from the CS measurements, a number of models have to be trained, each of which corresponds to a sampling rate. This may potentially degrade the performance of image CS, especially when multiple sampling rates are assigned to different blocks within an image. In this paper, we develop a multi-channel deep network for block-based image CS with performance significantly exceeding the current state-of-the-art methods. The significant performance improvement of the model is attributed to block-based sampling rates allocation and model-level removal of blocking artifacts. Specifically, the image blocks with a variety of sampling rates can be reconstructed in a single model by exploiting inter-block correlation. At the same time, the initially reconstructed blocks are reassembled into a full image to remove blocking artifacts within the network by unrolling a hand-designed block-based CS algorithm. Experimental results demonstrate that the proposed method outperforms the state-of-the-art CS methods by a large margin in terms of objective metrics, PSNR, SSIM, and subjective visual quality.

**Index Terms**—Block partition, blocking artifact, compressive sensing, deep network, image recovery.

## I. INTRODUCTION

Compressive sensing (CS), an emerging sampling and reconstructing strategy, can recover original signal from dramatically fewer measurements with a sub-Nyquist sampling rate [1]. As CS has the potentials of significantly improving the sampling speed and sensor energy efficiency, it has been applied in many practical applications, including single pixel imaging [2], fast magnetic resonance imaging [3], high-speed video cameras [4] and image encryption [5]. To deal with high-dimensional natural images efficiently, block-based CS is proposed as a lightweight CS approach [6]–[8]. In such strategy, a scene under view is partitioned into some small blocks, which are then sampled and reconstructed independently. Meaningful information is usually not uniformly distributed in an image, so the block partition benefits more fair allocation of the sensing resources for the whole image [9].

Although block-based CS enjoys the advantages of low-cost sampling, lightweight reconstruction, and capability of adaptively assigning sensing resources, it also usually suffers

from reduced quality of image reconstruction due to blocking artifacts [8], [10]. To address the issue, some methods using an iterative block-based CS algorithm (BCS) are proposed [6], [8]. In each iteration, the projection operation is used to build an approximation of each block, while denoising operation acts on the full image reassembled by the approximative blocks. Results demonstrate that the recovered image blocks can be improved, while blocking artifacts can also be ameliorated as the iterations progress. This approach, however, may increase the reconstructing time, since small blocks still need to be concatenated into large-size full images to remove blocking artifacts.

Inspired by the powerful learning ability of deep neural networks in image representation [11], [12], several network-based CS methods are proposed [13]–[17], which are significantly faster than the traditional CS reconstruction algorithms. Using a fully connected layer to mimic the CS sampling, the network models can jointly optimize the sampling matrix and the reconstruction process, improving the qualities of recovered images. Although the CS network models are carefully constructed to enhance learning capabilities, several specific models have to be trained with various sampling rates, ignoring the mutual relationships among them. Consequently, blocking artifacts still exist in the existing deep network methods [14], [16], [17], especially when the employed sampling rates are very low. Moreover, most network-based image CS methods are trained as a black box, ignoring structural insight of CS reconstruction algorithms. Consequently, the reconstruction accuracy is decreased.

In this paper, we propose a multi-channel deep learning architecture for casting BCS algorithm into a learning network. It can benefit from the speed and learning capacities of deep networks while retaining the advantages of the previous BCS algorithms. To facilitate description, we term the multi-channel deep architecture as BCS-Net, which consists of a channel-specific sampling network and a unified deep reconstruction network. The channel-specific architecture is specifically designed to handle block-based allocation of sensing resources. The blocks with various sampling rates can then be fed into the same deep reconstruction network to exploit inter-block correlation for removing blocking artifacts. We further divide the reconstruction network into a fixed number of residual layers, each of which corresponds to an iteration of the BCS algorithm. To enable training, a modified version of the famous DnCNN network designed in [18] is used to replace the denoising operation in traditional BCS approach, which easily

This work was supported by the National Natural Science Foundation of China (no. 61772447).

S. Zhou, Y. He, and C. Li are with College of Computer Science and Electrical Engineering, Hunan University, Changsha 410082 China (swzhou@hnu.edu.cn).

Y. Liu is with the Department of Computer Science and Engineering, the University of Texas at Arlington, TX 76019, USA.

propagates gradients.

Our contributions of the paper are summarized below:

- A multi-channel sampling architecture specifically for block-based image CS is designed. Using this multi-channel architecture, block-wise CS measuring processed with a variety of sampling rates can be integrated into a single model to utilize the correlation among the blocks with different CS sampling rates.
- A deep reconstruction architecture based on the BCS algorithm is proposed using block-wise approximation and full-image-based denoising.
- Performances of the proposed approaches are verified by extensive experiments on three widely used benchmark datasets. The results show that the proposed multi-channel deep network can significantly outperform the state-of-the-art CS methods and network-based ones in terms of both subjective and objective metrics.

The remainder of this paper is organized as follows. In Sec. II, the related work on CS methods and network-based methods are reviewed. Section III introduces the idea of block-wise approximation and full-image-based denoising in BCS algorithm, and presents an extended version of the well-known Damp algorithm. The proposed multi-channel deep architecture is presented in Sec. IV and test results on its performance are given in Sec. V. The last section concludes the paper.

## II. THE RELATED WORK

In this section, we present the background of CS theory, then review the representative work on block-based image CS and deep network approaches.

### A. Preliminary of CS theory

Compressive sensing consists of two main steps: sampling/measuring process and reconstructing process. Let  $\mathbf{x}$  and  $\Phi$  denote a sparse signal of size  $1 \times n$  and an  $m \times n$  measurement/sampling matrix, respectively. Then, the sampling process can be presented as

$$y = \Phi \mathbf{x}, \quad (1)$$

where  $y$  is the  $m$ -length measurement vector sampled from  $\mathbf{x}$ . If signal  $\mathbf{x}$  is not sparse but compressible, the sampling process has to be further deduced from Eq. (1). That is,  $y = \Phi \mathbf{x} = \Phi \cdot \psi \alpha = \phi \alpha_0 + v$ , where  $v$  represents measurement noise,  $\psi$  denotes the sparse transform,  $\alpha$  is the coefficient vector in the corresponding transform domain,  $\phi = \Phi \psi$ , and  $\alpha_0$  is considered as a sparse vector approximating to  $\alpha$ . In general, a natural image is not strictly sparse signal, but often approximately sparse in some sparse transform domain.

The process of reconstructing signal  $\mathbf{x}$  needs much more computational complexity than the sampling process. It has been proven in [1] that if the sampling matrix obeys the restricted isometry property (RIP), it is possible to recover  $\mathbf{x}$  by solving an  $l_1$ -norm optimization problem:  $\min \|\alpha\|_1$ , subjecting to  $\|y - \phi \alpha\|_2^2 \leq \lambda$ , even if  $m \ll n$ . Here  $\lambda$  is a small constant, and one has  $\mathbf{x} = \psi^{-1} \alpha$  when  $\mathbf{x}$  is a compressible signal.

In the past two decades, a number of CS reconstruction algorithms have been developed, including basis pursuit [19], orthogonal matching pursuit [20], and the latest iteration-based Damp algorithm [21]. Although these algorithms enjoy solid mathematical foundations, they usually need long reconstructing time due to high computational complexity.

### B. Block-based image CS

Block-based CS is more effective for processing natural images because of increased dimensionality of such signals [6], [8], [22]. The scene under view is partitioned into relatively smaller non-overlapping blocks. The measurement matrixes corresponding to the small-size blocks are observed. Then, the image is sampled and reconstructed on a block-by-block basis [8]. This block-independent approach results in a reduced computational complexity for reconstruction with a much simplified sampling process.

As shown in Fig. 1, the meaningful information in different blocks of an image is non-uniform. Depending on the volume of information contained in each block, different sampling rates are adopted to reduce the overall sampling rate. Taking the two images in Fig. 1 as an example, lower CS sampling rates can be allocated for the block marked ‘‘C’’ in the image ‘‘Cameraman’’ and block ‘‘G’’ in image ‘‘Parrot’’.

As a consequence, sensing resources should be reasonably allocated to each block, instead of equally assigned. In [9], less sampling rates are allocated to non-salient image blocks but more to salient ones using the characteristics of human visual system. Concretely, a low-resolution sensor is used produce an initially sampled image, such that the adaptive sampling can be achieved for the input scene. In [23], the CS procedure is initialized with a low fixed-rate pre-sampling and an initial recovery. Then, the important regions are extracted by computing the saliency map of the initially recovered image. The adaptive CS strategy is further validated on some real video sequences [24]. In [25], we also propose an asymmetric approach to ensure fairer allocation of sampling rates among image blocks.

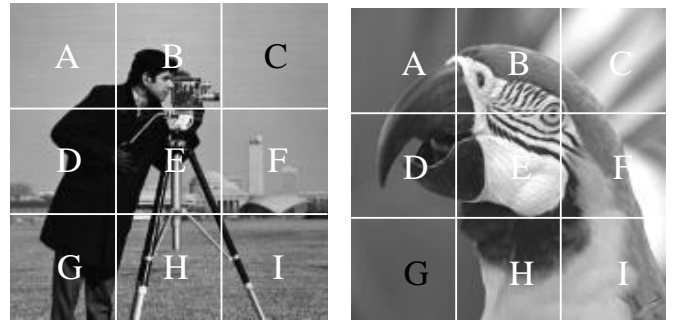


Fig. 1: Dividing two images for allocation of the sensing resources.

Due to the fact that block partition breaks the global correlation of the whole image, block-based CS prone to generate reconstructed image of low quality. In [6], an iterative BCS reconstruction approach is proposed to remove the blocking artifacts. The recovered images via BCS algorithm are

approximated on a block-by-block basis, but hard-thresholding denoising in each iteration is imposed on the full image, not image blocks. As a result, the artifacts incurred by block partition can be smoothed as the iteration progress. However, this can result in substantially increasing reconstruction complexity because of full-image denoising, which violates the motivation of lightweight design.

### C. Deep network approach for image CS

The tremendous success of deep learning in computer vision as shown in [11], [12] attracted application of deep neural networks in image CS [14], [15], [17], [26]. When an imaging system acquires CS measurements, the reconstructing process is performed with a deep network. Compared with the traditional CS, deep network approaches generally enjoy much faster reconstruction speed, while still achieving high-quality recovered images owing to their significant learning capabilities.

In [14], a network-based ReconNet approach is introduced to learn the inverse mapping from block-wise CS measurements to their desired image blocks. It is further improved in [16] that the measurement matrix and the reconstruction process are jointly learned. In [15], [17], traditional CS algorithms and deep networks are blended by treating parameters of the algorithm as weights to be learned. Unfortunately, full-image reconstruction is prone to overfitting due to the potentially overwhelming number of parameters of the sampling layer. So block-independent image recovery has to be performed instead of reconstructing the full image directly. As a consequence, blocking artifacts can be observed in the recovered images. To address the issue, the recovered images are fed into the BM3D denoiser designed in [27] to remove blocking artifact [14], [16]. However, the benefit of using an traditional off-the-shelf denoiser is not convincingly demonstrated.

For each sampling rate, the corresponding network model has to be trained to learn the inverse CS mapping. This may be not desirable for block-based CS, since a large number of model parameters need to be stored. In [15], a neural network architecture is applied to a variety of measurement matrices. Unfortunately, its performance improvement is less significant than traditional CS methods because the measurement matrices cannot participate in the network training. Inspired by the multi-scale super-resolution method given in [28], [29] introduce a multi-scale CS approach, where the main network is shared across multiple sampling rates. However, their method only reuses a portion of parameters, and a CS sampling rate still correspond to a specific network model. In other words, they do not consider block partition and the corresponding problem of blocking artifacts.

## III. BLOCK-WISE APPROXIMATION AND FULL-IMAGE-BASED DENOISING

In this section, we first introduce the key idea of the popular BCS algorithm [6], i.e., block-wise approximation and full-image-based denoising. Then we propose an extended version of the well known Damp approach [21] by exploiting this idea.

### A. Block-wise approximation and full-image-based denoising in BCS

The BCS algorithm is an iterative reconstruction approach specialized for block-based image CS. It solves the image reconstruction problem by using approximation with projection onto the convex set and hard thresholding denoising in the iteration process, as shown in

$$\begin{cases} r_i^{t+1} = \hat{x}_i^t + \Phi_B^*(y_i - \Phi_B \hat{x}_i^t), \\ \hat{X}^{t+1} = \mathcal{H}(R^{t+1}), \end{cases} \quad (2)$$

where  $\Phi_B$  is the measurement matrix corresponding to a block and  $\Phi_B^*$  is its pseudo-inverse,  $r_i^{t+1}$  denotes the  $(t+1)^{th}$  approximation of the recovered block  $\hat{x}_i$ , and all  $\{r_i^{t+1}\}_{i=1}^K$  are reassembled into a full image  $R^{t+1}$ . Here we assume that the original image are divided into  $K$  blocks,  $y_i$  is the measurement sampled from block  $x_i$ . The reconstruction starts from some initial approximation  $\hat{X}^0$  and forms the recovered image  $\hat{X}^{t+1}$  at  $(t+1)^{th}$  iteration. In the BCS approach,  $\mathcal{H}(\cdot)$  represents hard thresholding, which is widely used in removing Gaussian noise. In the special case when  $\Phi_B$  is an orthonormal matrix, we can deduce that  $\Phi_B^* = \Phi_B^T$ , where  $\Phi_B^T$  is the transpose of  $\Phi_B$ .

We can conclude that, the key idea of BCS algorithm is block-wise approximation, as illustrated in the first equation in (2). The denoising operation, on the contrary, is imposed on the full image, not each block, as shown in the second equation in (2). In this way, blocking artifacts can be removed while still maintaining block-wise CS sampling.

### B. BCS-Damp algorithm

Inspired by BCS algorithm, in this subsection, we propose an extension for Damp algorithm, called BCS-Damp, to reconstruct the images with block partition.

Damp is a state-of-the-art CS reconstruction algorithm, which is also an iterative approach like BCS. Let  $\Phi$  be the measurement matrix of image  $x$ , and  $y$  is the corresponding measurements. Damp algorithm takes the form

$$\begin{cases} z^t = y - \Phi \hat{x}^t + z^{t-1} \text{div}(\hat{x}^t)/m, \\ (\hat{\sigma}^t)^2 = \|z^t\|_2^2 / m, \end{cases} \quad (3)$$

where  $\hat{x}^t = \mathcal{D}_{\hat{\sigma}^{t-1}}(\hat{x}^{t-1} + \Phi^* z^{t-1})$ . The part  $\hat{x}^t + \Phi^* z^t$  in Eq. (3) can be written as  $x + v^t$ , where  $x$  is the original image and  $v^t$  can be regarded as a Gaussian noise at iteration  $t$ .  $\hat{\sigma}^t$  is an estimate of the standard deviation of that Gaussian noise.  $m$  is the number of CS measurements.  $\text{div}D(\cdot)$  denotes the operation of partial derivative, and  $\text{div}D_{\hat{\sigma}^t}$  represents the divergence of the denoiser.

However, Damp is not specially designed for block-based CS, and correspondingly it does not consider blocking artifacts as a result. With the idea of BCS in mind, that is, block-wise approximation is employed to decrease computation complexity, while full-image-based denoising is imposed to remove blocking artifacts, we propose an extension of Damp for

block-based image CS. Our proposed BCS-Damp algorithm is illustrated as

$$\begin{cases} r_i^{t+1} = \hat{x}_i^t + \Phi_B^* \cdot z_i^t, \\ z_i^t = y_i - \Phi_B \hat{x}_i^t + z_i^{t-1} \{\text{div} \mathcal{D}_{\hat{\sigma}^{t-1}}(R^t)\}_i / m, \\ \hat{X}^{t+1} = \mathcal{D}_{\hat{\sigma}^t}(R^{t+1}), \end{cases} \quad (4)$$

where  $\{\cdot\}_i$  represents the  $i^{\text{th}}$  block in an image. Here we maintain the operation of  $\text{div} \mathcal{D}_{\hat{\sigma}^{t-1}}$  in Damp algorithm. The modification we have to introduce is that,  $\mathcal{D}_{\hat{\sigma}^t}(\cdot)$  does not run on the blocks, but on the full image  $R^{t+1}$ , obtained by concatenating all approximated blocks  $\{r_i^{t+1}\}_{i=1}^K$ , as shown in the last equation in (4).

In the following section, block-wise approximation but full-image-based denoising, along with the iterative structure of BCS algorithm, will be further casted into a carefully designed deep network for removing artifacts and improving the recovered image.

#### IV. MULTI-CHANNEL DEEP NETWORK ARCHITECTURE

In this section, we propose a multi-channel deep network architecture, termed BCS-Net, to reconstruct the images acquired by block-wise CS sampling. The proposed BCS-Net is composed of a multi-channel sampling network and a deep reconstructing network, as shown in Fig. 2. These two networks consist of an integrated end-to-end model, of which the learnable parameters are jointly trained by our proposed two-stage training strategy.

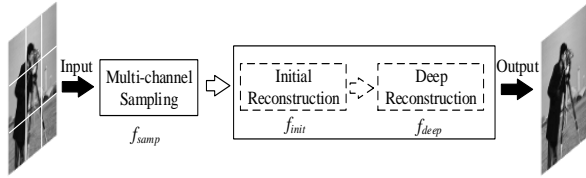


Fig. 2: BCS-Net architecture, which is composed of a multi-channel sampling network and a reconstruction network including an initial reconstruction part and a deep reconstruction part.

##### A. Multi-channel sampling architecture

This subsection investigates a  $k$ -channel network architecture, named  $f_{\text{samp}}$ , to mimic the adaptive sampling process of block-based CS, as shown in Fig. 3.

The proposed  $f_{\text{samp}}$  has  $k$  channels, each of which corresponds to a sampling rate assigned to a specific image block. A higher value of  $k$  indicates a more detailed division of sampling rates of image blocks, thereby block partition can benefit the fairer allocation of the sensing resources, but resulting in more complex sampling architecture. The full scene under view,  $X$ , is partitioned into  $K$  non-overlapping image blocks of size  $B \times B$ . Using the schematic image  $X$  in Fig. 3 as an example,  $K$  is set to 9. According to CS theory, for image block  $x_i$ , the sampling process can be represented as  $y_i = \Phi_{B,j} \cdot x_i$ . Here  $\Phi_{B,j}$  ( $1 \leq j \leq k$ ) is the  $m_j \times n_B$  measurement matrix of block  $x_i$ ,  $n_B = B^2$ ,  $1 \leq i \leq K$ , and

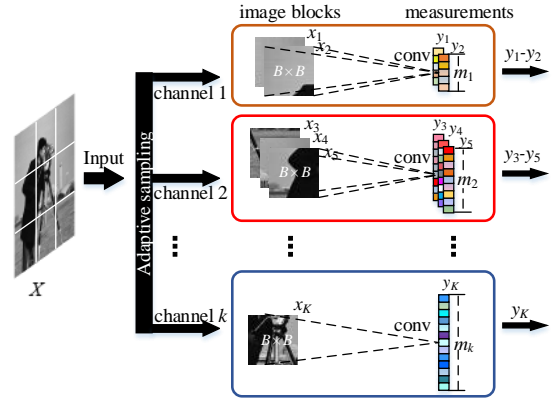


Fig. 3:  $k$ -channel sampling network  $f_{\text{samp}}$ , with which the blocks with different sampling rates are fed into the network via their respective channels.

$y_i$  is the corresponding measurements. We have  $m_j = s_j \cdot n_B$ , where  $s_j$  is the sampling rate assigned to block  $x_i$ . With our sampling network, a channel is related to a sampling rate, and  $k$  channels can then correspond to a number of target sampling rates by employing linear combination of those  $k$  sampling rates.

For the  $j^{\text{th}}$  channel in  $f_{\text{samp}}$ , we use a convolutional layer, in which we do not set bias and activation, to mimic the sampling process. This convolutional layer is defined as  $w_j^{\text{samp}} \otimes x_i$ , where  $w_j^{\text{samp}}$  denotes  $m_j$  convolution kernels of size  $B \times B \times 1$ . In other words,  $w_j^{\text{samp}}$  corresponds to measurement matrix  $\Phi_{B,j}$ . Note that the measurements among different channels are different from each other, since each channel corresponds to its own convolutional kernel. However, the blocks within the same image are spatially correlated. As a consequence, the measurements of those blocks among different channels are related to each other. If  $x_i$  is fed into  $j^{\text{th}}$  channel, we have

$$y_i = f_{\text{samp}}(x_i, w_j^{\text{samp}}). \quad (5)$$

The size of the convolution kernel  $w_j^{\text{samp}}$  depends on the sampling rate  $s_j$  and the size of image blocks. We should note that, compared with traditional measurement matrix, the weights of  $w_j^{\text{samp}}$  are learnable. In this perspective, it is more rigorous that network-based CS approaches should be referred to as the ones inspired by CS, instead of being CS.

We note that  $k$  channels in our sampling network corresponds to  $k$  sampling rates, respectively, and  $k$  may be less than  $K$ , the total number of the blocks in an image. With our multi-channel model, the blocks have to be measured via their respective channels, and the number of the channels,  $k$ , is then related to the number of blocks of an image,  $K$ . Ideally, a block corresponds to a unique channel. In this case, we have  $k = K$ . If several blocks within an image are similar to each other, such as those blocks belonging to the background, they can be considered to assign the same sampling rates. At this point, we have  $k < K$ . Fortunately, all  $k$  channels can be trained sufficiently in the training process, since we have enough training images, and thus each of these  $k$  channels

will receive enough training blocks regardless of the allocation strategies employed.

Obviously, if the full image is not partitioned into blocks, too many parameters may be needed to store the weights and it will be easily prone to overfitting. This may also be the main reason that most existing deep network approaches reconstruct the full image with block-by-block strategy. In this paper, we are going to further investigate the problem of blocking artifacts due to block partition.

### B. Deep reconstructing architecture

In this subsection, we construct a deep reconstruction architecture to cast the idea of iterative block-wise approximation but full-image-based denoising into the network, achieving model-level removal of blocking artifacts. Our deep architecture is composed of an initial reconstruction network  $f_{\text{init}}$  and a deep reconstruction network  $f_{\text{deep}}$ , as shown in Fig. 4.

The initial reconstruction network,  $f_{\text{init}}$ , has  $k$  inputs, each of which corresponds to a sampling channel in  $f_{\text{samp}}$  as illustrated in Section IV-A. The  $j^{\text{th}}$  ( $1 \leq j \leq k$ ) input is connected to the corresponding  $j^{\text{th}}$  convolutional layer, which uses  $B^2$  kernels of size  $1 \times 1 \times m_j$  and generates  $B^2$  values by convolving them with  $y_i$ . Here  $y_i$  is the measurement of block  $x_i$  entering  $j^{\text{th}}$  channel. All these  $B^2$  values are combined into one  $B \times B$  feature map,  $\hat{x}_i^0$ , and we refer to it as the initially reconstructed result of block  $x_i$ . From the network's point of view, we have

$$\hat{x}_i^0 = f_{\text{init}}(y_i, w_j^{\text{init}}), \quad (6)$$

where  $w_j^{\text{init}}$  denotes the above mentioned  $1 \times 1 \times m_j$  convolutional kernel corresponding to the  $j^{\text{th}}$  channel in the sampling network. As we can see from Fig. 4, our initial reconstruction network includes only one convolutional layer for simplification reason, and the initially recovered images is going to be improved by our deep reconstruction network.

The proposed deep reconstruction network,  $f_{\text{deep}}$ , is further divided into  $T$  phases, so that the iterative BCS algorithm can be unrolled along with these  $T$  phases. In  $f_{\text{deep}}$ , each phase corresponds to one iteration in BCS algorithm consisting of approximation and denoising operations. At  $(t+1)^{\text{th}}$  phase the block-wise approximation is implemented by using a formula slightly different from (2) in Sec. III-A, as shown in

$$r_i^{t+1} = \hat{x}_i^t + \Phi_{B,j}^*(y_i - \Phi_{B,j} \hat{x}_i^t) \quad (7)$$

for each block  $x_i$ , where  $\Phi_{B,j}$  is the measurement matrix specialized for block  $x_i$ , if  $x_i$  is fed into the network via  $j^{\text{th}}$  channel in our multi-channel sampling model. Note that the matrix  $\Phi_{B,j}$  is learnable, and it may be not an orthogonal matrix. Thus, its pseudo-inverse,  $\Phi_{B,j}^*$ , can not be simplified into  $\Phi_{B,j}^T$  as in the traditional BCS or Damp algorithm.

We then reassemble all approximated blocks  $\{r_i^{t+1}\}_{i=1}^K$  to build a full, approximated image,  $R^{t+1}$ , for further denoising processing. To enable training of the deep reconstruction network, we modify the famous DnCNN network to implement full-image denoising. Traditional denoising methods, such as hard thresholding in BCS and BM3D in Damp algorithm, will not work in deep network architecture, since they cannot

propagate gradients. This restricts us to focus on feed-forward convolutional neural networks. DnCNN is our choice, which fortunately offers improved performance on image deblocking and Gaussian denoising. Our deep reconstruction network is composed of  $T$  phases. Each phase has 5 convolutional layers, and the configuration is designed by referring to the DnCNN network. The first layer generates  $d$  feature maps with the  $d$  kernels of size  $f \times f \times 1$ , and last layer generates 1 feature map with one  $f \times f \times d$  kernel. All three other layers employ  $d$  kernels, each of which is of the size of  $f \times f \times d$ . It should be noted that all conventional layers explore the RELU activation function except the last layer. In DnCNN, 20 convolutional layers are employed to form a deep network for image denoising. In our network model, 5 convolutional layers form a phase, and  $T$  phases are employ to deal with both image denoising and image approximation. In our experiments,  $d$ ,  $f$  and  $T$  are set to 64, 3 and 10, respectively. Let  $w_t^{\text{deep}}$  be the parameters of convolutional kernels in  $t^{\text{th}}$  phase. Then one has

$$\hat{X}^T = f_{\text{deep}}(R^1, \{w_t^{\text{deep}}\}_{t=1}^T), \quad (8)$$

where  $R^1$  is the approximated image in the first phase in the deep network.

### C. Two-stage training

We propose to divide the training process into two stages to improve the recovered images by training sampling matrix  $\{\Phi_{B,j}\}_{j=1}^k$  while being able of utilizing  $\{\Phi_{B,j}^*\}_{j=1}^k$  in deep reconstruction process.

As illustrated in Section IV-A, in our network sampling matrixes  $\{\Phi_{B,j}\}_{j=1}^k$  are implemented by employing convolution operations. That is, the elements in  $\Phi_{B,j}$  and  $\Phi_{B,j}^*$  have to be taken from the convolution kernel in the  $j^{\text{th}}$  channel in the sampling network. However, we find that, if both  $\Phi_{B,j}$  and  $\Phi_{B,j}^*$  participate in the training process, we cannot achieve a desired recovered image. This is because, in the training process,  $\Phi_{B,j}$  has to be updated in real time along with each back propagation. Unfortunately, back propagation is based on the gradient decent rule, which will be hindered due to the real-time computing of  $\Phi_{B,j}^*$  in the deep reconstruction network.

In view of this, in the first stage, we aim to obtain the training parameters of the sampling network. That is, we have to achieve  $k$  optimal sampling matrices  $\{\Phi_{B,j}\}_{j=1}^k$  and the corresponding matrices  $\{\Phi_{B,j}^*\}_{j=1}^k$ . It is observed that, our deep architecture consists of an initial reconstruction network  $f_{\text{init}}$  without including  $\Phi_{B,j}^*$  and a deep reconstruction network  $f_{\text{deep}}$  where  $\Phi_{B,j}^*$  is utilized to improve the recovered images. In this way, we combine the sampling network and the initial reconstruction part of our reconstruction network into a training network, i.e.,  $f_{\text{init}}(f_{\text{samp}}(\cdot), \cdot)$ , which is used to train the sampling matrix  $\{\Phi_{B,j}\}_{j=1}^k$ . Given the training images  $\{X_n\}_{n=1}^N$ , the cost function  $L_{\text{samp}}$  is

$$L_{\text{samp}} = \frac{1}{2N} \sum_{n=1}^N \|f_{\text{init}}(f_{\text{samp}}(X_n, \{w_j^{\text{samp}}\}_{j=1}^k), \{w_j^{\text{init}}\}_{j=1}^k) - X_n\|^2, \quad (9)$$

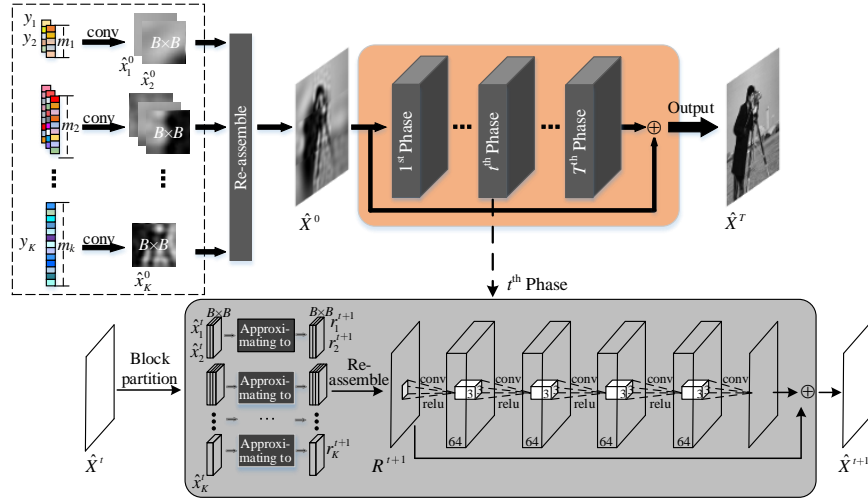


Fig. 4: Deep reconstruction architecture, in which the image is approximated by block at each residual phase, while these approximated blocks are reassembled into a full image to perform denoising by employing a modified version of DnCNN phase by phase.

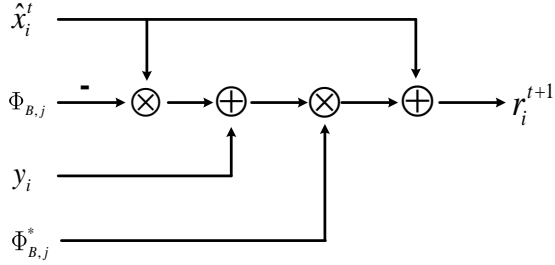


Fig. 5: Deep reconstruction .

where  $N$  is the number of images in the training dataset.

In the second stage, we further train the reconstructing network consisting of an initial reconstruction part and a deep reconstruction part, i.e.,  $f_{\text{deep}}(f_{\text{init}}(\cdot), \cdot)$ , where the parameters in  $\{\Phi_{B,j}^*\}_{j=1}^k$  come from  $\{\Phi_{B,j}\}_{j=1}^k$ . That is, the sampling weights  $\{w_j^{\text{samp}}\}_{j=1}^k$  are fixed while the parameters  $\{\{w_j^{\text{init}}\}_{j=1}^k, \{w_t^{\text{deep}}\}_{t=1}^T\}$  are updated in the training process. Our reconstructing network  $f_{\text{deep}}(f_{\text{init}}(\cdot), \cdot)$  directly learns the mapping between the CS measurements and the ground truth, and the loss function minimizing the error between the input and the output is on the basis of full images instead of image blocks. Mean square error is adopted to design an end-to-end cost function

$$L_{\text{deep}} = \frac{1}{2N} \sum_{n=1}^N \| f_{\text{deep}}(f_{\text{init}}(\{y_{i,n}\}_{i=1}^K, \{w_j^{\text{init}}\}_{j=1}^k), \{w_t^{\text{deep}}\}_{t=1}^T) - X_n \|_2^2, \quad (10)$$

where  $y_{i,n}$  denotes the CS measurement vector of the  $i^{\text{th}}$  block in  $n^{\text{th}}$  training image.

## V. PERFORMANCE EVALUATION

In this section, we conduct extensive experiments to evaluate the performance of the proposed BCS-Net and BCS-Damp

schemes, and compare them with state-of-the-art methods, including traditional BCS [6], Damp [21], network-based Ista [17], ReconNet [14] and its improved version, I-Recon [16], in terms of reconstruction quality, time complexity and visual effect.

### A. Training and testing

1) *Constructing a training set:* The training images are from the training set (200 images) and testing set (200 images) of the BSDS500 database [30], in which we randomly crop 89600 images with the size of  $96 \times 96$  as the training set. Each training image,  $X$ , is further partitioned into 9 image blocks of size  $32 \times 32$ ,  $\{x_i\}_{i=1}^9$ . That is, there are a total of 806400 blocks in our training set. Visual saliency of the scene was exploited in [9], [31]. In the experiments, the methods in reference [9] is used to compute the saliency map of training images. Suppose that  $v$  represents the amount of the saliency information embodied in image  $X$ . Then we have  $v = \frac{1}{n} \sum_{j \in X_s} l_j$ , where  $n$  is the total number of pixels on image  $X$ ,  $X_s$  denotes the saliency map of  $X$ , and  $l_j$  is the saliency value of location  $j$  on  $X_s$ . Let  $v_i$  be the saliency information of image block  $x_i$ , and  $p_i = \frac{v_i}{v}$  denotes the proportion of the saliency information of block  $x_i$ . We can then construct the training data pair for our network, as shown in

$$(X, \{(x_i, p_i)\}_{i=1}^K). \quad (11)$$

where  $K = 9$  and there are a total of  $N = 89600$  training image pairs.

For three existing network-based approaches, Ista, ReconNet and I-Recon, 806400 image blocks are randomly cropped. These blocks and themselves consists of 806400 training block pairs for training, since these approaches are all based on block-independent image recovery.

2) *Training details:* We set  $k = 7$  for our  $k$ -channel network model, and the sampling rates are in the

range of  $\{0.01, 0.03, 0.05, 0.1, 0.2, 0.3, 0.4\}$ . Each image pair  $(X, \{(x_i, p_i)\}_{i=1}^9)$  is further processed in order to find out the most appropriate channels in the network. For a given target sampling rate ( $SR$ ), we calculate sub-rate  $s_i$  of block  $x_i$  as

$$s_i = SR \cdot p_i \cdot \frac{n}{n_B}, \quad (12)$$

where  $p_i$  is defined in Section V-A1,  $n$  and  $n_B$  are the sizes of an image and its block, respectively. In the training process, the space of sampling rates is divided into seven intervals, each of which corresponds to a channel. If  $s_i$  falls within the interval  $[T_c, T_{c+1}]$  corresponding to  $c^{th}$  channel, then block  $x_i$  is pushed into the network via channel  $c$ .

In the experiment, we train the network with 50 epoches. The batch size is set to 1, since each image have to be partitioned into 9 blocks and these blocks are reassembled in our multi-channel network. The mean square error between the original image and the output of the network is calculated as the loss for back-gradient propagation. Adam optimization [32] with a learning rate of 0.0001 is adopted to optimize the parameters. We use TensorFlow 1.4 [33] to train the proposed multi-channel network at a desktop platform configured with one NVIDIA 1060 GPU, one CPU @ 4.00 GHz of Intel(R) Core (TM) i7-4790K and 32GB of memory. The training processes takes about 3 hours for one epoch.

3) *Testing set*: We test our multi-channel networks with three widely used benchmark datasets, Set5, Set11 and BSD100, where Set5 and Set11 are shown in Fig. 5 and Fig. 6, respectively.

Set5 consists of 5 gray images, where the sizes of “Bird” and “Head” are  $288 \times 288$ , “Baby”, “Butterfly” and “Woman” are with the size of  $512 \times 512$ ,  $256 \times 256$  and  $224 \times 352$ , respectively. Set11 has 11 gray images, where the sizes of “Fingerprint” and “Flintstones” are  $512 \times 512$ , and the other 9 images are all with the size of  $256 \times 256$ . BSD100 includes 100 images with the size of  $320 \times 480$  or  $480 \times 320$ . These test images are with a various types of spatial distribution of key visual information. For example, the main meaningful information in images “Cameraman” and “Parrot” in Set11 is located in the single connected region. In contract, the visual information of “Bird” in Set5, “Fingerprint”, “Flintstones” and “Peppers” in Set11 uniformly distributes in the whole images. Note that all those test images are strictly separate from the training datasets.



Fig. 6: Five typical images owning different spatial information distribution: a) “Baby”; b) “Bird”; c) “Butterfly”; d) “Head”; e) “Woman”.

## B. Results and analysis

1) *Comparisons with the state-of-the-art methods*: In this subsection, we evaluate the performance of the proposed BCS-Net with adaptive allocation of sampling rate and BCS-Damp, and compare them with the existing methods.

For our BCS-Net, all test images are reprocessed to simulate the initial CS sampling by conforming to the following simulations. Each original test image is first resized to one percent of its original size, which mimics the scene under view pre-sampled by a low-resolution imaging sensor. After that, the saliency of the pre-sampled image is computed. This small-size saliency map is further normalized and bilinearly interpolated to a map with the original size. The saliency information of the original test images,  $v$ , is then estimated. As a consequence, the sampling resources can be allocated to all blocks by using (12), instead of being equally allocated.

To guarantee the average rate of the sampling rates corresponding to each channel being equal or close to the target rate,  $SR$ , the following procedure is employed. As with the training process, the space of sampling rates is first divided into seven intervals. The  $c^{th}$  interval corresponds to  $c^{th}$  channel, and is represented as  $[T_c, T_{c+1}]$ , where  $1 \leq c \leq k$  and  $k$  is the total number of channels in our multi-channel model. Then we compute the sampling rate  $s_i$  for  $i^{th}$  block by using (12), where  $1 \leq i \leq b$  and  $b$  is the total number of blocks. If  $s_i$  falls into the interval  $[T_c, T_{c+1}]$ , the value of  $s_i$  is changed to  $c_t$ . Here  $c_t$  is the sampling rate corresponding to  $c^{th}$  channel and  $1 \leq t \leq k$ . If  $\sum_{i=1}^b s_i = b \cdot SR$ , then the average sampling rate of all block is exactly equal to the target sampling rate. Otherwise, we carry out fine tune by changing some blocks to the higher or lower channel according to the positive or negative difference, i.e.,  $b \cdot SR - \sum_{i=1}^b s_i$ . We should note that the average sampling rates can be very close to the target rates, and thus we ignore the differences between them in the experiments.

The average PSNR (peak signal-to-noise ratios) and SSIM (structural similarity index) with BCS-Net are reported in Table I. The comparison of running times of reconstructing the images in Set5 and Set11 is shown in Table II. Here the running times are the average values of all 16 test images in Set5 and Set11 with the sampling rate of 0.1. We should note that, 0.1 is the target sampling rate of an image, and our running time contains the time of reconstructing all blocks with different channels in the multi-channel architecture.

The best performance is labeled in bold, the second best is italic, and the second best is underlined.

As shown in Table I, our BCS-Net yields higher-quality recovered image in terms of both PSNR and SSIM than other existing methods, including BCS, Damp, ReconNet, I-Recon, and Ista, for Set5, Set11, and BSD100, respectively. From Table I, we can easily observe a significant performance improvement of, for instance, 3.82 dB and 2.98 dB on Set5 and Set11 with the sampling rate of 0.1, and 2.95 dB on BSD 100 with the sampling rate of 0.2, respectively. We notice that, along with the increase of the sampling rate, the improvement of our scheme slows down. The possible cause is that, when the sampling rate is as high as 0.1 or 0.2, the recovered images for the competing approach are of relatively high quality. And there is not too much space for improvement with even more



Fig. 7: Elven images with a variety of spatial information distribution in Test dataset ‘‘Set11’’.

TABLE I: The average PSNR in dB and SSIM on Set5, Set11 and BSD100 with a range of sampling rates.

Set5 (PSNR/SSIM)							
Sampling rate	0.01	0.03	0.05	0.1	0.2	0.3	0.4
Algorithm							
BCS [6]	16.20/0.3613	20.80/0.5088	22.54/0.5974	24.87/0.7280	28.50/0.8130	30.54/0.8539	32.32/0.8899
Damp [21]	6.51/0.0311	19.95/0.4821	21.56/0.5667	24.24/0.6997	28.49/0.8527	32.29/0.9137	34.25/0.9395
<b>BCS-Damp</b>	19.97/0.4827	22.28/0.6267	24.10/0.6962	27.95/0.8247	32.47/0.9105	36.46/0.9397	39.53/0.9565
ReconNet [14]	18.46/0.4492	21.54/0.5699	23.33/0.6462	25.70/0.7422	28.16/0.8197	30.03/0.8620	31.00/0.8793
I-Recon [16]	21.49/0.5571	25.00/0.7113	26.97/0.7908	28.49/0.8329	30.53/0.8823	34.51/0.9403	35.30/0.9465
Ista [17]	18.06/0.4589	21.50/0.5624	25.15/0.7307	28.89/0.8405	33.21/0.9152	36.00/0.9456	38.14/0.9622
<b>BCS-Net (WA)</b>	<b>22.98/0.6103</b>	<b>26.69/0.7702</b>	<b>28.72/0.8371</b>	<b>31.86/0.9034</b>	<b>35.43/0.9488</b>	<b>37.87/0.9681</b>	<b>39.88/0.9785</b>
<b>BCS-Net</b>	<b>22.98/0.6103</b>	<b>27.09/0.7699</b>	<b>28.81/0.8237</b>	<b>32.71/0.9030</b>	<b>36.12/0.9483</b>	<b>38.64/0.9694</b>	<b>39.88/0.9785</b>
Set11 (PSNR/SSIM)							
Sampling rate	0.01	0.03	0.05	0.1	0.2	0.3	0.4
Algorithm							
BCS [6]	15.65/0.3973	19.40/0.5146	20.89/0.5768	23.15/0.6836	25.74/0.7778	27.78/0.8331	29.75/0.8783
Damp [21]	5.49/0.0582	18.47/0.4986	20.14/0.5588	22.73/0.6873	26.85/0.8335	30.09/0.8994	32.93/0.9339
<b>BCS-Damp</b>	18.53/0.4692	21.03/0.5795	22.61/0.6471	26.20/0.7919	30.75/0.8976	34.21/0.9415	37.09/0.9648
ReconNet [14]	16.99/0.4145	19.80/0.5110	21.14/0.5935	23.28/0.6896	25.54/0.7719	27.11/0.8155	28.32/0.8411
I-Recon [16]	19.80/0.5018	22.59/0.6540	24.54/0.7442	25.97/0.7888	27.92/0.8457	31.45/0.9135	32.26/0.9243
Ista [17]	16.55/0.4139	19.74/0.5154	22.83/0.6792	26.49/0.8010	30.79/0.8950	33.76/0.9345	36.03/0.9547
<b>BCS-Net (WA)</b>	<b>20.88/0.5505</b>	<b>24.05/0.7048</b>	<b>25.89/0.7851</b>	<b>28.63/0.8628</b>	<b>32.08/0.9220</b>	<b>34.65/0.9506</b>	<b>36.70/0.9662</b>
<b>BCS-Net</b>	<b>20.88/0.5505</b>	<b>24.47/0.7807</b>	<b>26.04/0.7723</b>	<b>29.43/0.8676</b>	<b>33.06/0.9283</b>	<b>35.60/0.9554</b>	<b>36.70/0.9662</b>
BSD100 (PSNR/SSIM)							
Sampling rate	0.01	0.03	0.05	0.1	0.2	0.3	0.4
Algorithm							
BCS [6]	18.53/0.4213	20.93/0.4797	21.54/0.4996	23.21/0.5843	25.04/0.6742	26.48/0.7384	27.75/0.7875
Damp [21]	7.00/0.0495	19.57/0.4260	20.54/0.4706	21.92/0.5333	24.29/0.6286	26.00/0.6970	27.57/0.7541
<b>BCS-Damp</b>	19.90/0.4255	21.58/0.4896	22.47/0.5216	24.10/0.5842	26.48/0.6745	28.79/0.7490	31.44/0.8184
ReconNet [14]	18.74/0.3960	20.56/0.4647	21.52/0.5120	23.00/0.5837	24.68/0.6694	25.83/0.7204	26.71/0.7611
I-Recon [16]	21.15/0.4654	23.09/0.5662	24.19/0.6320	25.35/0.7098	26.87/0.7872	29.24/0.8593	30.07/0.8812
Ista [17]	17.86/0.3957	20.47/0.4699	22.65/0.5692	24.79/0.6726	27.64/0.7906	29.86/0.8580	31.70/0.9003
<b>BCS-Net (WA)</b>	<b>22.03/0.4997</b>	<b>24.10/0.6085</b>	<b>25.16/0.6709</b>	<b>26.97/0.7651</b>	<b>29.52/0.8609</b>	<b>31.59/0.9107</b>	<b>33.44/0.9405</b>
<b>BCS-Net</b>	<b>22.03/0.4997</b>	<b>24.43/0.6108</b>	<b>25.58/0.6669</b>	<b>27.84/0.7709</b>	<b>30.59/0.8672</b>	<b>32.64/0.9160</b>	<b>33.44/0.9405</b>

TABLE II: The average time for reconstructing the images in Set5 and Set11 with the sampling rate of 0.1 (in second).

Algorithm	BCS	Damp	BCS-Damp	ReconNet	I-Recon	Ista	BCS-Net(WA)	BCS-Net
Time	100s	228s	611s	0.87s	0.89s	1.05s		2.02s

sampling rates.

We can also see from Table I that, in existing methods I-Recon has relatively better reconstruction quality at extremely low sampling rates of 0.01, 0.03 and 0.05, while Ista usually performs better at the sampling rates of 0.2 and above. However, our BCS-Net always outperforms the traditional BCS and Damp algorithms, as well as the network-based ReconNet, I-Recon and Ista algorithms. We think that, the performance improvement of our scheme is mainly due to the following two factors, i.e., adaptive allocation of sampling rate in our multi-channel sampling network, and block-wise approximation and full-image denoising in our deep reconstruction network. We notice that BCS-Net has slightly longer running time than network-based ReconNet, I-Recon and Ista because of our multi-channel sampling and block reassembling, but it runs significantly far faster than optimization-based BCS and Damp reconstruction algorithm.

The proposed BCS-Damp approach also outperforms Damp and BCS algorithm, as shown in Table I. This is because,

compared with Damp algorithm, in our BCS-Damp, BM3D denoising is imposed on the full image instead of each block, and blocking artifacts can then be ameliorated. And compared with BCS approach, our BCS-Damp has better denoising performance, since BM3D denoising outperforms the hard thresholding employed in BCS approach. We notice that the proposed BCS-Damp even outperforms BCS-Net in terms of PSNR for Set11 at very high sampling rate of 0.4. We think this is another indication that network-based approaches generally offer more advantages over relatively lower sampling rates. Note that our BCS-Damp has much longer running time than BCS and Damp due to our full-image denoising strategy in the iteration process and relatively higher computation complexity of BM3D denoising algorithm.

2) *Performance evaluation without assigning sampling resources:* In this subsection, we evaluate the performance of our BCS-Net scheme without assigning sampling rate (WA), since the sensing resources may not be allocated in certain scenarios. That is, all blocks in an image are assigned the



TABLE III: Detailed comparison of PSNR in dB and SSIM in the range of [0, 1] on the images of Set5.

Images	SR	BCS	Damp	BCS-Damp	ReconNet	I-Recon	Ista	BCS-Net	BCS-Net(WA)
Baby	0.01	18.20/0.4838	4.46/0.0288	24.29/0.6615	21.19/0.5582	24.22/0.6430	20.87/0.5778	<b>26.35/0.6988</b>	<b>26.35/0.6988</b>
	0.03	24.60/0.7020	23.37/0.6554	25.50/0.7403	24.24/0.6482	27.88/0.7614	23.67/0.6347	<b>30.66/0.8274</b>	29.59/0.8013
	0.05	26.10/0.7646	25.30/0.7265	27.34/0.7850	25.77/0.7084	29.80/0.8294	27.68/0.7671	<b>32.07/0.8689</b>	31.27/0.8493
	0.1	28.81/0.8684	27.37/0.8034	29.90/0.8746	28.03/0.7749	30.86/0.8605	30.23/0.8381	<b>34.72/0.9137</b>	33.63/0.9075
	0.2	31.57/0.9328	30.10/0.8968	33.73/0.9502	30.56/0.8459	32.58/0.8997	33.25/0.9055	<b>37.74/0.9579</b>	36.52/0.9525
	0.3	33.31/0.9583	32.95/0.9508	37.38/0.9760	31.93/0.8770	36.12/0.9451	35.52/0.9410	<b>39.94/0.9755</b>	38.59/0.9715
	0.4	34.89/0.9730	34.91/0.9732	<b>40.56/0.9872</b>	32.84/0.8911	36.65/0.9461	37.41/0.9611	40.52/0.9822	40.52/0.9822
Bird	0.01	17.90/0.3885	8.33/0.0225	19.98/0.4757	19.38/0.4609	22.14/0.5726	19.00/0.4628	<b>23.35/0.6391</b>	<b>23.35/0.6391</b>
	0.03	20.72/0.4550	20.87/0.4850	22.35/0.6164	22.25/0.6085	26.07/0.7543	22.49/0.5930	27.60/0.7871	<b>27.98/0.8142</b>
	0.05	23.70/0.6481	21.67/0.5280	24.43/0.7029	24.32/0.6827	28.22/0.8325	26.32/0.7657	28.96/0.8286	<b>30.55/0.8832</b>
	0.1	26.67/0.7584	25.27/0.7030	29.40/0.8570	27.02/0.7964	30.25/0.8942	31.20/0.8852	<b>34.88/0.9369</b>	34.40/0.9454
	0.2	30.41/0.8583	31.50/0.8963	37.51/0.9644	29.71/0.8740	32.70/0.9350	36.83/0.9576	<b>39.60/0.9770</b>	39.20/0.9790
	0.3	33.22/0.9085	36.89/0.9623	42.26/0.9862	32.12/0.9148	37.65/0.9745	40.50/0.9785	<b>42.69/0.9889</b>	42.29/0.9895
	0.4	35.50/0.9362	37.21/0.9753	<b>45.56/0.9928</b>	33.22/0.9308	38.62/0.9788	43.10/0.9867	<b>44.67/0.9937</b>	44.67/0.9937
Butterfly	0.01	11.98/0.2601	5.23/0.0006	13.08/0.3317	13.36/0.2766	15.47/0.3802	12.97/0.2851	<b>15.68/0.4078</b>	<b>15.68/0.4078</b>
	0.03	14.88/0.3615	13.10/0.3215	15.28/0.4779	15.77/0.4041	19.36/0.6211	15.71/0.4032	21.01/0.6988	20.62/0.7046
	0.05	16.32/0.4330	14.98/0.4477	17.41/0.5913	17.52/0.5319	21.58/0.7326	19.31/0.6666	<b>23.56/0.7947</b>	23.55/0.8211
	0.1	18.71/0.5545	17.65/0.6308	22.21/0.7999	20.11/0.6581	22.78/0.7511	24.56/0.8479	<b>27.94/0.8968</b>	27.46/0.9015
	0.2	21.44/0.6622	22.80/0.8348	26.84/0.8994	22.74/0.7596	24.85/0.8200	30.17/0.9355	30.96/0.9386	<b>31.24/0.9504</b>
	0.3	23.50/0.7233	26.46/0.9052	29.99/0.9375	24.80/0.8227	29.54/0.9286	33.66/0.9604	<b>33.98/0.9680</b>	33.67/0.9698
	0.4	25.26/0.7698	29.77/0.9387	34.24/0.9648	25.81/0.8401	30.34/0.9362	<b>36.50/0.9741</b>	<b>35.60/0.9791</b>	35.60/0.9791
Head	0.01	17.60/0.3134	9.44/0.0964	24.62/0.4831	21.33/0.5025	25.30/0.6133	21.08/0.5199	<b>28.19/0.6603</b>	<b>28.19/0.6603</b>
	0.03	24.79/0.5102	24.42/0.4616	27.37/0.6304	25.09/0.6025	28.21/0.6939	25.54/0.6128	<b>30.73/0.7368</b>	30.54/0.7351
	0.05	25.97/0.5512	26.65/0.5626	28.62/0.6692	26.97/0.6408	29.71/0.7469	19.31/0.6831	<b>31.96/0.7813</b>	31.74/0.7792
	0.1	29.86/0.7232	28.50/0.6380	30.31/0.7282	28.90/0.7115	30.88/0.8091	30.82/0.7561	<b>33.89/0.8426</b>	33.60/0.8400
	0.2	31.74/0.7876	31.17/0.7610	32.37/0.7926	30.41/0.7694	32.46/0.8574	33.34/0.8352	<b>35.99/0.8996</b>	35.81/0.8977
	0.3	33.10/0.8320	32.67/0.8036	33.50/0.8238	32.08/0.8054	35.51/0.8975	35.07/0.8819	<b>37.71/0.9311</b>	37.43/0.9285
	0.4	34.27/0.8650	33.92/0.8380	34.55/0.8513	32.53/0.8276	36.02/0.9100	36.38/0.9117	<b>38.85/0.9485</b>	<b>38.85/0.9485</b>
Woman	0.01	15.29/0.3608	5.10/0.0074	17.89/0.4613	17.06/0.4475	20.30/0.5762	16.41/0.4490	<b>21.30/0.6457</b>	<b>21.30/0.6457</b>
	0.03	19.01/0.5153	18.01/0.4867	20.92/0.6684	20.32/0.5861	23.47/0.7258	20.08/0.5684	<b>25.44/0.7995</b>	24.71/0.7958
	0.05	20.63/0.5902	19.19/0.5684	22.72/0.7325	22.06/0.6674	25.55/0.8125	23.97/0.7711	<b>27.50/0.8450</b>	26.48/0.8529
	0.1	24.13/0.7354	22.41/0.7235	27.95/0.8640	24.45/0.7702	27.67/0.8497	27.62/0.8753	<b>32.12/0.9247</b>	30.22/0.9226
	0.2	27.36/0.8242	26.88/0.8747	31.88/0.9456	27.36/0.8497	30.06/0.8994	32.46/0.9421	<b>36.30/0.9684</b>	34.37/0.9645
	0.3	29.55/0.8724	32.50/0.9465	<b>39.19/0.9751</b>	29.23/0.8898	33.77/0.9557	35.24/0.9661	<b>38.90/0.9835</b>	37.38/0.9811
	0.4	31.64/0.9053	35.46/0.9722	<b>42.74/0.9865</b>	30.59/0.9068	34.90/0.9615	37.32/0.9773	<b>39.74/0.9888</b>	39.74/0.9888

same sampling rate, and accordingly, they are fed into our model from the same channel corresponding to the target rate. In this case, our multi-channel architecture becomes a unified deep network for  $k$  target sampling rates. In the simulation,  $k$  is set to 7, and these seven channels are in a range of  $\{0.01, 0.03, 0.05, 0.1, 0.2, 0.3, 0.4\}$ . The comparison of average PSNR and SSIM of recovered Set5, Set11 and BSD100 can be observed in Table I. The detailed comparison of PSNR and SSIM for Set5 and Set11 is illustrated in Table III and IV, where we omit the results of testing set BSD100 due to limited space.

We should note that, our multi-channel model decreases large amount of storage requirements, since we use a unified deep reconstruction network to serve all sampling rates. For instance, Ista approach for seven different sampling rates has about 0.34 million (M) parameters each, totaling 2.4M, while our reconstruction network has only 1.1M parameters.

Table I shows that, the proposed WA scheme still achieves higher PSNR and SSIM than the best results of the existing BCS, Damp, ReconNet, I-Recon and Ista, thanks to the strategy of block-wise approximation and full-image based denoising. We can see from Table I that, our WA scheme always has lower PSNR than the proposed BCS-Net with adaptive allocation at the sampling rates of  $\{0.03, 0.05, 0.1, 0.2, 0.3\}$  for Set5, Set11 and BSD100. We also notice that, for Set5, our WA scheme achieves slightly better SSIM than BCS-Net with adaptive allocation. From Table III, IV, the qual-

ity gap between BCS-Net and BCS-Net (WA) increases in some images, but decreases in other images. For example, the gap of recovered ‘‘Cameraman’’ and ‘‘Parrot’’ is about  $28.02-26.06=1.96(\text{dB})$  and  $31.14-28.39=2.59(\text{dB})$ , but it drops to  $25.29-25.03=0.26(\text{dB})$  and  $26.36-24.49=-0.13(\text{dB})$  for ‘‘Flintstones’’ and ‘‘Fingerprint’’ with sampling rate of 0.1, respectively. This is because, the foreground objects of ‘‘Cameraman’’ and ‘‘Parrot’’ can be clearly distinguished from background information. In other words, the main meaning information in these images is limited to some local regions. As a consequence, the average assignment of sampling rate is obviously less efficient than adaptive allocation. However, the meaning information in ‘‘Flintstones’’ and ‘‘Fingerprint’’ is almost uniformly distributed in their respective image, and thus the effect of adaptive allocation is not so obvious. From Table I, our WA scheme has the same values of PSNR and SSIM with adaptive allocation at the target rates of 0.01 and 0.4. The reason is, in our experiment 0.01 and 0.4 are set to be minimal and maximal sampling rates respectively. According to (12) illustrated in Section V-A2, the adaptive allocation strategy degenerate to equal allocation, i.e., WA scheme.

3) *Comparison of visual effects*: Using test image ‘‘Parrot’’ as an example, this section gives the visual effect of recovered images with our BCS-Net, BCS-Damp and other existing methods.

As shown in Fig. 8(a), in the case of very low sampling rate of 0.03, the proposed BCS-Net has obviously better visual

TABLE IV: Detailed comparison of PSNR in dB and SSIM in the range of [0, 1] on the images of Set11.

Images	SR	BCS	Damp	BCS-Damp	ReconNet	I-Recon	Ista	BCS-Net	BCS-Net(WA)
House	0.01	17.70/0.5555	5.01/0.0704	21.76/0.6336	19.10/0.5401	22.16/0.6125	19.30/0.5487	<b>23.65/0.6767</b>	<b>23.65/0.6767</b>
	0.03	22.04/0.6457	20.59/0.6651	25.74/0.7618	22.47/0.6046	25.51/0.7173	22.48/0.6034	<b>29.76/0.8128</b>	28.28/0.7914
	0.05	23.70/0.6766	24.38/0.7092	28.53/0.8049	24.00/0.6678	27.70/0.7814	26.68/0.7607	<b>31.21/0.8413</b>	30.29/0.8281
	0.1	26.36/0.7372	27.25/0.7951	32.45/0.8525	26.55/0.7398	29.06/0.8016	30.55/0.8366	<b>33.62/0.8795</b>	32.75/0.8734
	0.2	29.72/0.8104	32.12/0.8540	35.48/0.8828	28.90/0.7927	30.96/0.8430	35.10/0.8921	<b>37.30/0.9183</b>	36.23/0.9134
	0.3	31.49/0.8390	35.05/0.8833	38.12/0.9326	30.40/0.8220	34.42/0.8984	37.17/0.9198	<b>38.62/0.9386</b>	38.16/0.9360
	0.4	33.92/0.8921	37.08/0.9177	<b>40.15/0.9532</b>	31.57/0.8379	35.24/0.9057	38.67/0.9400	<b>39.71/0.9557</b>	<b>39.71/0.9557</b>
Cameraman	0.01	16.56/0.4689	6.33/0.1057	17.98/0.4725	17.01/0.4502	19.65/0.5543	16.33/0.4624	<b>20.38/0.6148</b>	<b>20.38/0.6148</b>
	0.03	18.70/0.5384	17.64/0.5119	20.52/0.6318	19.12/0.5225	21.65/0.6490	19.44/0.5151	<b>23.56/0.7430</b>	22.64/0.7117
	0.05	20.05/0.5863	18.95/0.5920	21.68/0.6760	20.08/0.5774	23.00/0.7143	20.82/0.6598	<b>25.43/0.7935</b>	23.82/0.7666
	0.1	21.71/0.6478	20.92/0.6640	24.44/0.7635	21.76/0.6553	23.81/0.7380	23.50/0.7559	<b>28.02/0.8612</b>	26.06/0.8376
	0.2	24.30/0.7380	23.67/0.7711	28.54/0.8463	23.27/0.7194	25.43/0.7948	27.46/0.8556	<b>30.74/0.9142</b>	29.05/0.9004
	0.3	25.97/0.7880	26.33/0.8266	30.97/0.8805	24.60/0.7618	28.12/0.8739	30.20/0.9025	<b>32.44/0.9392</b>	31.11/0.9285
	0.4	27.90/0.8334	27.86/0.8570	<b>34.50/0.9435</b>	25.53/0.7853	29.03/0.8862	32.25/0.9274	<b>32.62/0.9463</b>	<b>32.62/0.9463</b>
Parrot	0.01	17.58/0.5604	5.85/0.0690	20.09/0.6576	17.26/0.5491	20.75/0.6509	16.75/0.5325	<b>22.23/0.7164</b>	<b>22.23/0.7164</b>
	0.03	20.46/0.6447	20.16/0.6586	22.14/0.7185	20.53/0.6197	22.79/0.7377	20.41/0.6269	<b>25.35/0.8229</b>	24.23/0.8014
	0.05	22.30/0.7160	21.23/0.6935	23.45/0.7705	21.68/0.6868	24.53/0.8031	23.32/0.7585	<b>27.87/0.8638</b>	25.50/0.8405
	0.1	24.05/0.7771	22.83/0.7693	28.12/0.8563	23.52/0.7562	26.03/0.8293	26.72/0.8499	<b>31.14/0.9126</b>	28.39/0.8957
	0.2	26.21/0.8375	25.60/0.8418	32.90/0.9073	25.84/0.8171	28.00/0.8731	29.54/0.9101	<b>34.36/0.9496</b>	31.67/0.9389
	0.3	28.18/0.8754	28.19/0.8878	35.55/0.9351	27.20/0.8453	31.35/0.9286	32.92/0.9398	<b>36.90/0.9668</b>	34.71/0.9602
	0.4	30.00/0.9057	30.82/0.9169	<b>38.17/0.9574</b>	28.38/0.8648	31.85/0.9344	35.41/0.9579	<b>37.23/0.9736</b>	<b>37.23/0.9736</b>
Peppers	0.01	14.53/0.4051	5.78/0.0621	17.37/0.5129	16.57/0.4309	19.20/0.5369	15.94/0.4263	<b>20.67/0.6088</b>	<b>20.67/0.6088</b>
	0.03	17.96/0.4620	18.58/0.5333	19.93/0.6371	19.36/0.5086	22.28/0.6969	19.47/0.5328	23.69/0.7542	<b>23.90/0.7607</b>
	0.05	20.99/0.5872	19.87/0.5936	21.58/0.6839	20.63/0.6023	24.15/0.7776	22.49/0.6901	24.87/0.7996	<b>25.46/0.8254</b>
	0.1	23.76/0.6694	22.60/0.7055	25.97/0.7939	22.91/0.7002	25.26/0.7986	27.28/0.8170	<b>28.35/0.8897</b>	28.30/0.8868
	0.2	24.86/0.6751	28.10/0.8371	31.10/0.8854	25.02/0.7691	26.91/0.8459	32.52/0.9075	<b>31.99/0.9305</b>	<b>32.08/0.9337</b>
	0.3	26.83/0.7374	31.01/0.8925	34.85/0.9262	26.73/0.8167	31.33/0.9141	<b>35.45/0.9383</b>	<b>34.59/0.9506</b>	34.38/0.9502
	0.4	29.88/0.8303	34.02/0.9213	<b>37.08/0.9435</b>	28.00/0.8349	31.27/0.9214	<b>37.47/0.9537</b>	<b>36.10/0.9617</b>	<b>36.10/0.9617</b>
Boats	0.01	16.46/0.3843	5.46/0.0593	19.42/0.4605	18.29/0.4089	20.85/0.4837	17.54/0.4058	<b>22.05/0.5402</b>	<b>22.05/0.5402</b>
	0.03	20.66/0.4870	17.82/0.4902	21.55/0.5623	20.97/0.5073	23.95/0.6375	20.95/0.5030	<b>25.67/0.7043</b>	25.27/0.6946
	0.05	21.31/0.5552	20.78/0.5396	23.21/0.6315	22.48/0.5823	25.80/0.7234	23.93/0.6708	<b>27.54/0.7777</b>	27.27/0.7782
	0.1	22.65/0.6355	23.46/0.6514	26.27/0.7502	24.55/0.6790	27.55/0.7891	27.46/0.7966	<b>30.39/0.8679</b>	30.01/0.8672
	0.2	24.54/0.7426	27.76/0.8147	31.41/0.8873	26.93/0.7698	29.60/0.8565	31.94/0.9057	<b>33.67/0.9244</b>	<b>33.49/0.9326</b>
	0.3	28.59/0.8024	31.11/0.8973	35.87/0.9469	28.61/0.8256	33.04/0.9234	35.27/0.9479	<b>36.14/0.9546</b>	<b>35.69/0.9550</b>
	0.4	30.49/0.8506	35.55/0.9471	<b>39.14/0.9702</b>	29.76/0.8509	34.02/0.9335	37.75/0.9668	<b>37.63/0.9686</b>	<b>37.63/0.9686</b>

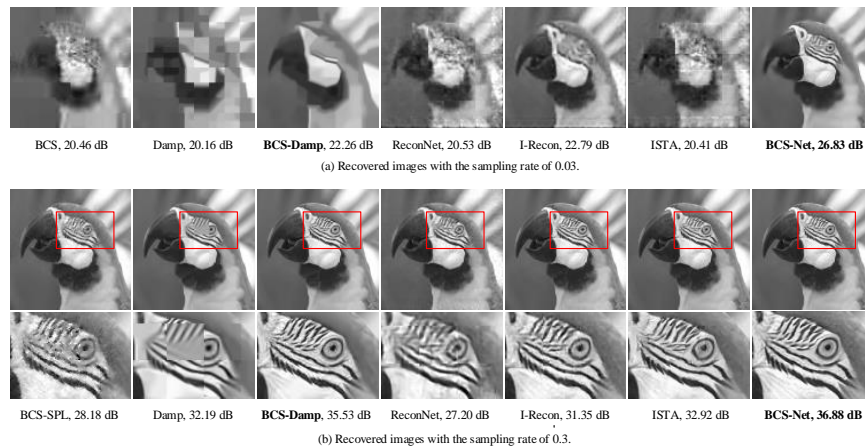


Fig. 8: Comparison of visual effect of the recovered “Parrot” with different sampling rates: a) 0.03; b) 0.3.

effect than other approaches. We can observe significant blocking artifacts in recovered “Parrot” with traditional Damp and network-based Ista, ReconNet and I-Recon. This is because all these algorithms reconstruct “Parrot” block by block, without consideration of blocking artifacts due to block partition. We also notice that the block artifacts in BCS and our proposed BCS-Damp are not so obvious as other competing methods. The reason is that, in BCS and BCS-Damp, block-wise approximation is interleaved with full-image-based denoising, and the artifacts can then be gradually ameliorated as iterations progress. Our BCS-Net synthesizes the common merits of BCS

algorithm and deep network approach, and thus achieves the best performance.

As we can see from Fig. 8(b), when the sampling rate increases to 0.3, the recovered “Parrot” with seven approaches are all improved. However, we can still observe obvious blocking artifacts for Damp and ReconNet algorithms. With I-Recon and Ista, some weak blocking artifacts are also noted. Compared with those competing approaches, our BCS-Net is capable of reconstructing more details and sharper edges, and has not more blocking artifacts.

TABLE V: Detailed comparison of PSNR in dB and SSIM in the range of [0, 1] on the images of Set11.

Images	SR	BCS	Damp	BCS-Damp	ReconNet	I-Recon	Ista	BCS-Net	BCS-Net(WA)
Monarch	0.01	13.38/0.3399	6.25/0.0462	14.94/0.3961	14.69/0.3612	17.43/0.4803	14.35/0.3708	<b>17.82/0.4981</b>	<b>17.82/0.4981</b>
	0.03	16.68/0.4536	15.51/0.4449	17.77/0.5305	17.92/0.5005	21.11/0.6781	17.40/0.4917	<b>23.30/0.7287</b>	<b>22.72/0.7409</b>
	0.05	18.43/0.5281	17.05/0.5321	20.01/0.6324	19.06/0.5875	23.47/0.7758	21.13/0.6930	24.65/0.7718	<b>25.54/0.8295</b>
	0.1	21.08/0.6369	20.09/0.6519	24.07/0.7821	21.82/0.7020	24.61/0.8016	25.53/0.8366	<b>29.32/0.8937</b>	<b>28.86/0.9065</b>
	0.2	24.14/0.7480	24.87/0.8413	28.76/0.9005	24.45/0.7960	26.67/0.8620	30.98/0.9335	<b>33.23/0.9527</b>	<b>32.77/0.9563</b>
	0.3	26.79/0.8144	28.49/0.9181	32.79/0.9499	26.24/0.8468	31.03/0.9396	34.87/0.9640	<b>36.11/0.9743</b>	<b>35.30/0.9742</b>
	0.4	28.49/0.8527	31.76/0.9519	<b>37.98/0.9750</b>	27.54/0.8685	31.91/0.9481	37.73/0.9766	<b>37.35/0.9826</b>	<b>37.35/0.9826</b>
Foreman	0.01	18.06/0.5834	4.92/0.1082	23.52/0.7136	19.71/0.5991	23.68/0.6997	19.00/0.5895	<b>26.22/0.7565</b>	<b>26.22/0.7565</b>
	0.03	24.22/0.7102	23.81/0.7271	28.49/0.8314	23.77/0.6807	27.15/0.8056	23.5/0.6740	<b>30.68/0.8442</b>	<b>30.70/0.8579</b>
	0.05	25.95/0.7359	26.06/0.7846	30.96/0.8664	30.96/0.7466	29.33/0.8534	28.49/0.8272	<b>32.35/0.8752</b>	<b>32.35/0.8886</b>
	0.1	29.04/0.8149	30.64/0.8518	33.78/0.9066	27.79/0.8039	29.90/0.8549	33.18/0.8995	<b>35.85/0.9325</b>	<b>35.18/0.9293</b>
	0.2	32.01/0.8674	34.74/0.9193	36.62/0.9325	30.03/0.8551	31.94/0.8892	37.75/0.9456	<b>39.00/0.9619</b>	<b>38.29/0.9608</b>
	0.3	34.48/0.9019	37.28/0.9396	38.80/0.9484	31.81/0.8802	35.96/0.9421	40.32/0.9647	<b>40.99/0.9753</b>	<b>40.23/0.9738</b>
	0.4	36.40/0.9253	38.60/0.9497	41.24/0.9649	32.73/0.8887	36.20/0.9425	41.77/0.9757	<b>42.33/0.9757</b>	<b>41.77/0.9811</b>
Barbara	0.01	16.89/0.3458	5.66/0.0402	19.38/0.4291	18.17/0.3727	20.82/0.4607	17.51/0.3665	<b>21.75/0.4959</b>	<b>21.75/0.4959</b>
	0.03	20.66/0.4694	19.53/0.4380	20.90/0.4804	20.43/0.4642	22.61/0.5813	20.32/0.4681	23.24/0.5996	<b>23.32/0.6216</b>
	0.05	21.31/0.5193	20.86/0.4716	21.71/0.5128	21.13/0.5157	23.40/0.6388	21.80/0.5661	23.64/0.6380	<b>23.75/0.6570</b>
	0.1	22.65/0.5961	22.36/0.5683	23.52/0.6199	22.20/0.5859	23.88/0.6915	23.53/0.6842	<b>24.73/0.7283</b>	<b>24.50/0.7270</b>
	0.2	24.53/0.7091	25.12/0.7253	29.26/0.8764	23.08/0.6525	24.75/0.7571	26.76/0.8331	<b>29.29/0.8805</b>	<b>26.64/0.8279</b>
	0.3	26.06/0.7814	29.76/0.8777	<b>35.40/0.9553</b>	23.87/0.7019	27.99/0.8616	30.76/0.9255	33.03/0.9479	30.78/0.9225
	0.4	27.47/0.8356	34.29/0.9527	<b>38.03/0.9735</b>	25.14/0.7598	29.56/0.8986	34.09/0.9606	34.23/0.9637	<b>34.23/0.9637</b>
Lena	0.01	14.79/0.3779	5.83/0.0700	19.35/0.5126	17.81/0.4427	21.02/0.5437	17.22/0.4371	<b>22.00/0.5956</b>	<b>22.00/0.5956</b>
	0.03	20.55/0.5481	19.66/0.5570	22.34/0.6565	20.94/0.5322	23.89/0.6788	20.91/0.5453	<b>25.88/0.7504</b>	25.64/0.7461
	0.05	22.41/0.6115	20.96/0.6153	23.80/0.7082	22.52/0.6285	25.85/0.7614	24.69/0.7265	26.11/0.7824	<b>27.15/0.8047</b>
	0.1	24.20/0.6803	24.19/0.7137	26.32/0.7794	24.45/0.7079	26.86/0.7957	27.69/0.8227	<b>30.62/0.8895</b>	<b>29.36/0.8737</b>
	0.2	26.43/0.7736	27.05/0.8172	30.93/0.8895	26.55/0.7825	28.82/0.8581	31.37/0.9067	<b>34.36/0.9481</b>	<b>32.29/0.9316</b>
	0.3	28.87/0.8301	29.01/0.8677	34.82/0.9432	27.99/0.8235	32.18/0.9261	33.83/0.9419	<b>36.71/0.9686</b>	<b>35.07/0.9612</b>
	0.4	30.44/0.8680	31.31/0.9063	<b>37.49/0.9655</b>	29.24/0.8521	33.13/0.9372	36.25/0.9622	<b>37.30/0.9755</b>	<b>37.30/0.9755</b>
Flintstones	0.01	12.23/0.2009	4.33/0.0060	14.50/0.2814	13.59/0.2421	16.13/0.3335	13.45/0.2500	<b>16.65/0.3800</b>	<b>16.65/0.3800</b>
	0.03	14.96/0.3500	14.48/0.3242	16.04/0.4268	15.87/0.3365	18.72/0.4968	15.92/0.3458	<b>19.74/0.5683</b>	<b>19.49/0.5664</b>
	0.05	15.07/0.3575	15.56/0.4251	17.21/0.5738	17.32/0.4397	20.51/0.6134	18.99/0.5629	<b>22.61/0.6708</b>	<b>21.38/0.6751</b>
	0.1	18.22/0.6299	17.64/0.6448	21.62/0.8325	19.65/0.5663	22.63/0.6929	23.47/0.7489	<b>25.29/0.8044</b>	<b>25.03/0.8065</b>
	0.2	20.99/0.7820	22.87/0.8816	28.20/0.9540	22.74/0.7061	25.37/0.7852	28.56/0.8586	<b>29.37/0.8792</b>	<b>29.23/0.8876</b>
	0.3	23.26/0.8617	27.51/0.9512	<b>30.47/0.9701</b>	24.59/0.7637	29.00/0.8758	30.86/0.8920	<b>31.63/0.9127</b>	<b>31.26/0.9141</b>
	0.4	25.18/0.9040	29.92/0.9690	<b>31.80/0.9761</b>	25.87/0.7915	29.73/0.8862	32.31/0.9142	<b>32.60/0.9300</b>	<b>32.60/0.9300</b>
Fingerprint	0.01	13.96/0.1487	4.93/0.0027	15.48/0.0913	14.74/0.1625	16.08/0.1634	14.64/0.1631	<b>16.29/0.1722</b>	<b>16.29/0.1722</b>
	0.03	16.78/0.3512	15.37/0.1338	15.89/0.1378	16.39/0.3438	<b>18.81/0.5152</b>	16.38/0.3629	18.30/0.4676	<b>18.32/0.4686</b>
	0.05	17.55/0.4712	15.89/0.1905	16.61/0.2580	17.87/0.4935	<b>22.23/0.7433</b>	18.83/0.5556	21.18/0.6812	<b>22.39/0.7430</b>
	0.1	19.68/0.6941	18.05/0.5441	21.64/0.7736	20.93/0.6896	26.04/0.8843	22.50/0.7626	26.36/0.8847	<b>26.49/0.8872</b>
	0.2	22.77/0.8718	23.46/0.8654	25.01/0.9111	24.18/0.8308	28.68/0.9383	26.76/0.8903	30.35/0.9513	<b>31.10/0.9590</b>
	0.3	25.06/0.9329	27.28/0.9515	28.72/0.9687	26.13/0.8829	31.55/0.9644	29.69/0.9426	<b>34.46/0.9806</b>	<b>34.47/0.9806</b>
	0.4	27.08/0.9633	31.03/0.9836	32.39/0.9900	27.77/0.9180	32.88/0.9738	32.10/0.9663	<b>37.19/0.9894</b>	<b>37.19/0.9894</b>

VI. CONCLUSION

In this paper, we further studied the problem of block-based image compressive sensing, and proposed a multi-channel deep neural network architecture, termed ‘BCS-Net’. The proposed architecture originates from the popular block-based CS algorithm, where block-wise iterative approximation together with full-image-based denoising is key for improving the recovered image. We then cast this idea into a carefully designed deep network, so that our proposed BCS-Net is capable of benefitting both from the learning capacities of deep network and from the hand-designed structure of BCS algorithm. Extensive experimental results show that our BCS-Net with adaptive sensing resource allocation achieves far better reconstruction quality and superb visual effect compared with state-of-the-art methods. At the same time, BCS-Net with WA approach also has excellent reconstruction performance with significantly reduced number of network parameters.

REFERENCES

[1] D. Donoho, “Compressed sensing,” *IEEE Transactions on Information Theory*, vol. 52, no. 4, pp. 1289–1306, 2006.

[2] M. F. Duarte, M. A. Davenport, D. Takhar, J. N. Laska, T. Sun, K. F. Kelly, and R. G. Baraniuk, “Single-pixel imaging via compressive sampling,” *IEEE Signal Processing Magazine*, vol. 25, no. 2, pp. 83–91, 2008.

[3] M. Lustig, D. L. Donoho, J. M. Santos, and J. M. Pauly, “Compressed sensing MRI,” *IEEE Signal Processing Magazine*, vol. 25, no. 2, pp. 72–82, 2008.

[4] Y. Hitomi, J. Gu, M. Gupta, T. Mitsunaga, and S. K. Nayar, “Video from a single coded exposure photograph using a learned over-complete dictionary,” in *IEEE International Conference on Computer Vision (ICCV)*, 2011, pp. 287–294.

[5] C. Li, Y. Zhang, and E. Y. Xie, “When an attacker meets a cipher-image in 2018: A Year in Review,” *Journal of Information Security and Applications*, vol. 48, p. art. no. 102361, 2019.

[6] L. Gan, “Block compressed sensing of natural images,” in *Proceedings of the International Conference on Digital Signal Processing*, 2007, pp. 403–406.

[7] S. Mun and J. E. Fowler, “Block compressed sensing of images using directional transforms,” in *IEEE International Conference on Image Processing (ICIP)*, 2009, pp. 3021–3024.

[8] J. Fowler, Sungkwang Mun, and E. Tramel, “Block-based compressed sensing of images and video,” *Foundations and Trends in Signal Processing*, vol. 4, no. 4, pp. 297–416, 2010.

[9] Y. Yu, B. Wang, and L. Zhang, “Saliency-based compressive sampling for image signals,” *IEEE Signal Processing Letters*, vol. 17, no. 11, pp. 973–976, 2010.

[10] K. Q. Dinh, H. J. Shim, and B. Jeon, “Measurement coding for compressive imaging using a structural measurement matrix,” in *IEEE International Conference on Image Processing (ICIP)*. IEEE, 2013, pp.

- 10–13.
- [11] A. Krizhevsky, I. Sutskever, and G. E. Hinton, “Imagenet classification with deep convolutional neural networks,” *Communications of the ACM*, vol. 60, no. 6, pp. 84–90, 2017.
  - [12] J. Long, E. Shelhamer, and T. Darrell, “Fully convolutional networks for semantic segmentation,” in *IEEE Conference on Computer Vision and Pattern Recognition (CVPR)*, 2015, pp. 3431–3440.
  - [13] A. Mousavi and R. G. Baraniuk, “Learning to invert: Signal recovery via deep convolutional networks,” in *IEEE International Conference on Acoustics, Speech and Signal Processing (ICASSP)*, 2017, pp. 2272–2276.
  - [14] K. Kulkarni, S. Lohit, P. Turaga, R. Kerviche, and A. Ashok, “Reconnet: Non-iterative reconstruction of images from compressively sensed measurements,” in *IEEE Conference on Computer Vision and Pattern Recognition (CVPR)*, 2016, pp. 449–458.
  - [15] C. Metzler, A. Mousavi, and R. Baraniuk, “Learned D-AMP: Principled neural network based compressive image recovery,” in *Proceedings of the 31st International Conference on Neural Information Processing Systems (NIPS’17)*, 2017, pp. 1770–1781.
  - [16] S. Lohit, K. Kulkarni, R. Kerviche, P. Turaga, and A. Ashok, “Convolutional neural networks for non-iterative reconstruction of compressively sensed images,” *IEEE Transactions on Computational Imaging*, vol. 4, no. 3, pp. 326–340, 2018.
  - [17] J. Zhang and B. Ghanem, “Ista-net: Interpretable optimization-inspired deep network for image compressive sensing,” in *IEEE Conference on Computer Vision and Pattern Recognition (CVPR)*, 2018, pp. 1828–1837.
  - [18] K. Zhang, W. Zuo, Y. Chen, D. Meng, and L. Zhang, “Beyond a Gaussian Denoiser: Residual Learning of Deep CNN for Image Denoising,” *IEEE Transactions on Image Processing*, vol. 26, no. 7, pp. 3142–3155, 2017.
  - [19] S. S. Chen, D. L. Donoho, and M. A. Saunders, “Atomic decomposition by basis pursuit,” *SIAM review*, vol. 43, no. 1, pp. 129–159, 2001.
  - [20] M. Yang and F. de Hoog, “Orthogonal matching pursuit with thresholding and its application in compressive sensing,” *IEEE Transactions on Signal Processing*, vol. 63, no. 20, pp. 5479–5486, 2015.
  - [21] C. A. Metzler, A. Maleki, and R. G. Baraniuk, “From denoising to compressed sensing,” *IEEE Transactions on Information Theory*, vol. 62, no. 9, pp. 5117–5144, 2016.
  - [22] K. Q. Dinh, H. J. Shim, and B. Jeon, “Small-block sensing and larger-block recovery in block-based compressive sensing of images,” *Signal Processing-Image Communication*, vol. 55, pp. 10–22, 2017.
  - [23] A. Akbari, D. Mandache, M. Trocan, and B. Granado, “Adaptive saliency-based compressive sensing image reconstruction,” in *IEEE International Conference on Multimedia & Expo Workshops (ICMEW)*, 2016, pp. 1–6.
  - [24] G. Warnell, S. Bhattacharya, R. Chellappa, and T. Başar, “Adaptive-rate compressive sensing using side information,” *IEEE Transactions on Image Processing*, vol. 24, no. 11, pp. 3846–3857, 2015.
  - [25] S. Zhou, S. Xiang, X. Liu, and H. Li, “Asymmetric block based compressive sensing for image signals,” in *IEEE International Conference on Multimedia and Expo (ICME)*, 2018, pp. 1–6.
  - [26] W. Shi, F. Jiang, S. Zhang, and D. Zhao, “Deep networks for compressed image sensing,” in *IEEE International Conference on Multimedia and Expo (ICME)*, 2017, pp. 877–882.
  - [27] K. Dabov, A. Foi, V. Katkovnik, and K. Egiazarian, “Image denoising by sparse 3-D transform-domain collaborative filtering,” *IEEE Transactions on Image Processing*, vol. 16, no. 8, pp. 2080–2095, 2007.
  - [28] B. Lim, S. Son, H. Kim, S. Nah, and K. M. Lee, “Enhanced deep residual networks for single image super-resolution,” in *IEEE Conference on Computer Vision and Pattern Recognition Workshops (CVPRW)*, 2017, pp. 1132–1140.
  - [29] W. Shi, F. Jiang, S. Liu, and D. Zhao, “Multi-scale deep networks for image compressed sensing,” in *IEEE International Conference on Image Processing (ICIP)*, 2018, pp. 46–50.
  - [30] P. Arbelaez, M. Maire, C. Fowlkes, and J. Malik, “Contour detection and hierarchical image segmentation,” *IEEE Transactions on Pattern Analysis & Machine Intelligence*, vol. 33, no. 5, pp. 898–916, 2011.
  - [31] L. Itti, C. Koch, and E. Niebur, “A model of saliency-based visual attention for rapid scene analysis,” *IEEE Transactions on Pattern Analysis & Machine Intelligence*, vol. 20, no. 11, pp. 1254–1259, 1998.
  - [32] D. P. Kingma and J. Ba, “Adam: A method for stochastic optimization,” in *International Conference for Learning Representations (ICLR)*, 2015.
  - [33] M. Abadi, P. Barham, J. Chen, Z. Chen, A. Davis, J. Dean, M. Devin, S. Ghemawat, G. Irving, M. Isard *et al.*, “Tensorflow: A system for large-scale machine learning,” in *12th USENIX Symposium on Operating Systems Design and Implementation (OSDI)*, 2016, pp. 265–283.